

Deep phenotyping platform for microscopic plant-pathogen interactions

1 **Stefanie Lück¹ and Dimitar Douchkov¹**

2 ¹Leibniz Institute of Plant Genetics and Crop Plant Research (IPK), D-06466 Seeland, Germany

3

4 **Author for correspondence:**

5 Dimitar Douchkov

6 Tel. +49 39482 52825

7 Email: douchkov@ipk-gatersleben.de

8

9 **Keywords: automated microscopy, barley, BluVision, Deep learning, microphenomics,**
10 **neuronal networks, pathogens, plant, powdery mildew, wheat.**

11

12 Word counts:

13 · Total main body: 5 684

14 · Summary: 200

15 · Introduction: 931

16 · Material and Methods: 1 205

17 · Results: 2 690

18 · Discussion: 657

19 Number of figures: 11 (color)

20 Tables: 7

21 Supporting information: 1 figure, 4 tables

22 1 Summary

- 23 • The initial phases of plant-pathogen interactions are critical since they are often decisive
24 for the successful infection. However, these early stages of interaction are typically
25 microscopic, making it challenging to study on a large scale.
- 26 • For this reason, using the powdery mildew fungi of cereals as a model, we have developed
27 an automated microscopy pipeline coupled with deep learning-based image analysis for the
28 high-throughput phenotyping of plant-pathogen interactions.
- 29 • The system can quantify fungal microcolony count and density, the precise area of the
30 secondary hyphae of each colony, and different morphological parameters. Moreover, the
31 high throughput and sensitivity allow quantifying rare microscopic phenotypes in a large
32 sample size. One of these phenotypes is the cryptic infection of non-adapted pathogens,
33 marking the hidden transition stages of pathogen adaptation and breaking the nonhost
34 barrier. Thus, our tool opens the nonhost resistance phenomenon to genetics and genomics
35 studies.
- 36 • We have developed an open-source high-throughput automated microscopy system for
37 phenotyping the initial stages of plant-pathogen interactions, extendable to other
38 microscopic phenotypes and hardware platforms. Furthermore, we have validated the
39 system's performance in disease resistance screens of genetically diverse barley material
40 and performed Genome-wide associations scans (GWAS), discovering several resistance-
41 associated loci, including conferring nonhost resistance.

42

43 2 Introduction

44 Public authorities and society, particularly in Europe, mostly agree about an agroecological
45 transition toward a chemical pesticide-free and GMO-free agriculture. However, this ambitious
46 aim might be challenged by increased outbreaks of new aggressive pathogens promoted by global
47 trade, monocultures, and climatic changes. As high as 40% of global crop production is lost due
48 to pests and diseases, regardless of the extensive use of pesticides (FAO, 2020). Therefore, reduced
49 chemical pesticide use without compensating measures will threaten global food safety to an
50 unacceptable level. One of the most sustainable and environmentally friendly alternatives to
51 chemical pesticides is employing the natural disease resistance of plants. This approach was

52 successfully used in the long history of crop breeding. Still, to meet the new challenges, the plant
53 breeders need to discover new disease resistance sources by digging deep into the genetic diversity
54 stored in the gene banks and germplasm collections worldwide by using more sensitive
55 phenotyping tools capable of discovering quantitative trait loci (QTLs) even with minimal effects
56 and low allele frequency.

57 The scientific community has identified this need and initiated precise and high-throughput
58 phenotyping tools to establish a new scientific discipline called phenomics. However, most of
59 these efforts were aimed at phenotyping on a larger object level, such as whole plants and canopy,
60 with an insufficient spatial resolution for detailed studies of the typically microscopic plant-
61 pathogen interactions. To contribute to this bottleneck's alleviation, we started developing a highly
62 automated phenotyping platform to cover the subcellular, tissue, and organ level of phenotyping.
63 The system for organ-level phenotyping on a macroscopic scale called *Macrobot*, and the
64 corresponding software framework (*BluVision Macro*), were published previously (Lück et al.,
65 2020; Lueck et al., 2020). This article is focused on the high-throughput microscopic system for
66 phenotyping on the cellular and subcellular level, named *BluVision Micro*.

67 The primary aim of the *BluVision* framework is the phenotyping of plant-pathogen interactions on
68 microscopic and macroscopic levels. As a model for the development was selected, the well-
69 established system of the powdery mildew fungus *Blumeria graminis* as a pathogen of barley and
70 wheat (Panstruga and Dodds, 2009; Spanu and Kamper, 2010; Douchkov et al., 2014).

71 *B. graminis* is the only species of the ascomycete genus *Blumeria*, the order of *Erysiphales*. They
72 are causing powdery mildew diseases on many different grass species. All *Blumeria graminis* are
73 obligate parasites with typically extremely specific host-specialization forms, called *formae*
74 *speciales* (*ff.spp.*), e.g., *B. graminis* f. sp. *tritici* (wheat powdery mildew, Bgt), and the *B. graminis*
75 f. sp. *hordei* (barley powdery mildew, Bgh) (Wyand and Brown, 2003). Typically the plants are
76 entirely immune against the non-adapted pathogens, e.g., barley is immune to Bgt and wheat to
77 Bgh. However, some plant genotypes may allow microscopic growth of non-adapted pathogens,
78 known as cryptic infection (Romero et al., 2018; Bourras et al., 2019; Bettgenhaeuser et al., 2021).
79 The barley/wheat - powdery mildew model provides several advantages to the researchers: the
80 fungus growth is fast and highly synchronized, the majority of the fungal biomass is located on
81 the leaf surface, with straightforward to observe structures. Furthermore, the fungus interacts only

82 with the uppermost layer of plant leaf cells, the epidermis, via a specialized intracellular feeding
83 organ called a haustorium (Huckelhoven and Panstruga, 2011). This system of reduced complexity
84 provides an excellent environment for studying plant-pathogen interactions on a microscopic scale.
85 However, full-size and multilevel microscopy images of large objects, such as leaf segments, are
86 typically significant portions of complex data that were only very limitedly accessible with
87 automated image analysis methods until recently. The situation improved dramatically with the
88 coming of age of machine learning (ML) methods that use analytical models to identify patterns
89 and make decisions with minimal human intervention (Mitchell, 1997; Voulodimos et al., 2018).
90 There are two main approaches to ML – supervised learning from pre-labeled data (Russell, 2010)
91 and unsupervised learning from unlabeled data (Hinton, 1999). The analysis of images usually
92 includes classification and segmentation steps. The image classification uses features (variables)
93 from images that help classify the objects. The image segmentation assigns labels to the individual
94 pixels, groups them into subgroups (image objects), and subtracts them from the background
95 (Stockman and Shapiro, 2001). Choosing meaningful classification features (feature engineering)
96 (Zheng and Casari, 2018) can be crucial for the success of image analysis. This work compares
97 two main methods - selecting features by human decision (handcrafted features) and automatically
98 extracting features using a convolutional neural network (CNN). CNN can automatically select
99 many features, which leads to more robust prediction models. The downside of the CNNs is the
100 requirement of large training datasets, where predictive models like Random forest (RF) with
101 carefully selected handcrafted features show satisfying results even on small training sets (Lin et
102 al., 2020). The optimal approach depends on the specific application and typically would require
103 preliminary testing of different methods.

104 Here we present the *BluVision Micro* system dedicated to phenotyping the initial stages of plant-
105 pathogen interactions using high-throughput automated microscopy and computer vision methods
106 for localization and quantification of microscopic fungal structures. Unlike the macroscopic
107 systems that typically quantify the disease's visible symptoms, the *BluVision Micro* delivers
108 precise information about the pathogen behavior, the host's early response to the pathogen attack,
109 and the fungus's biomass and growth, virtually eliminating the environment's effects.

110

111

112 **3 Related work**

113 The first software development for segmentation and quantifying secondary hyphae of *B. graminis*
114 *f. sp. hordein* (barley powdery mildew) was the HyphArea Tool (Seiffert and Schweizer, 2005;
115 Baum et al., 2011) . The software was developed in Python 2. It is based on a histogram-based
116 threshold for hyphae segmentation and a shape descriptor for classifying the regions of interest
117 (ROI).

118 **4 Material and methods**

119 **4.1 Plant and fungal material**

120 Barley cv. Golden Promise and cv. Morex, and wheat cv. Kanzler were grown in 12 cm pots with
121 IPK-soil substrate. The plants were incubated in a plant growth cabinet (Sanyo/Panasonic MLR-
122 352H-PE Versatile Environmental Test Chamber, white LED upgrade; Panasonic Healthcare Co.,
123 Ltd.) at controlled conditions (dark period of 8h, light period of 16h, 20°C and 60 RH%) for 7 days
124 or 14 days. The second leaves were harvested and mounted on 1% water agar (Phyto agar,
125 Duchefa, The Netherlands) plates supplemented by 20 mg/L benzimidazole as a senescence
126 inhibitor. The barley leaf segments were inoculated with the Bgh isolate CH4.8, and the wheat leaf
127 segments were inoculated with Bgt isolate FAL92315 at approximately 5 spores/mm² in an
128 inoculation tower. The fungus was stopped at 36-96 hours after inoculation (hai) by incubating the
129 leave segments in a clearing solution (7 mL 96% Ethanol and 1 mL Acetic acid) for 48 hours at
130 room temperature. After that, the fungal colonies were stained with Coomassie staining solution
131 (0.3% Coomassie R250, 7.5% (w/v) trichloroacetic acid, and 50% (v/v) methanol) for 5 minutes
132 and then washed several times with water. The prepared samples were mounted on microscope
133 slides with 50 % glycerol to avoid drying the leaves during image acquisition.

134 The material of the barley core collection of genotypes was grown, collected, and inoculated as
135 described in (Lück et al., 2020). In brief, the plants were grown in 24-well seedling trays, ten plants
136 of the same genotype per well, in a climatized greenhouse for 14 days. Leaf fragments from the
137 second leaf were harvested and mounted on standard 4-well microtiter plates, filled with 1% water
138 agar supplemented by 20 mg/L benzimidazole. The leaf fragments were inoculated, incubated, and
139 stained as described above.

140 **4.2 Image acquisition and analysis hardware**

141 The microscopy image data was acquired on a commercial *Zeiss AxioScan.Z1* high-performance
142 microscopy slide scanner and ZEN 3.0 (blue edition) software (Carl Zeiss AG). The imaging was
143 done in a bright field configuration with a *Hitachi HV-F202SCL* camera (3 CCD 1/1.8" progressive
144 scan color sensor with 1600x1200 effective pixels and 24-bit color depth), 1x camera adapter. As
145 scanning objective typically was used an EC Plan-Neofluar 5x/0.16 M27 with 0.16 NA (numerical
146 aperture) that provided a large depth of field (DoF), which was particularly advantageous for
147 scanning very thick and uneven objects as whole-leaf fragments and helped reduce the Z-stack
148 levels to only five by keeping the most fungal structure focus. The acquired image data was stored
149 in a CZI file container that combines all relevant image and meta information in one file. The
150 image data were analyzed on a Windows 10 Enterprise server with a double *Intel Xeon™ E5-2695*
151 processor with 36 physical cores and 512 GB RAM, allowing nearly real-time analysis if required.
152 The macroscopic image data were acquired six days after infection, as described in (Lück et al.,
153 2020). Monochrome images in all illumination modes were acquired separately and stored in 16-
154 bit TIFF image files.

155 **4.3 Software implementation**

156 The software *BluVision Micro* and all experiments were implemented in *Python 3.6* under
157 *Windows 10* operating system. The following free *Python* libraries were used for development:
158 *OpenCV-Python, NumPy, Pandas, Keras, Tensorflow, czifile, skimage, mahotas, joblib* and *Scikit-*
159 *learn*. Training of the CNN model was done on NVIDIA TITAN X GPU with *Keras 2.3.1* and
160 *Tensorflow 2.1.0* backend, and training time of about 20.000 images per hour on an Intel® Core™
161 i7-9700 CPU 3.00 GHz with 64-Bit Windows 10 operation system.

162 The software is implemented as a two-step command-line tool with separated image processing
163 and data analysis, allowing curation of the intermediate results without rerunning the entire
164 analysis. In addition, the images processing can be parallelized, depending on the installed
165 computer memory.

166

167

168 **4.4 Barley Genotyping**

169 Two hundred barley accessions from the barley collection of the Federal *ex-situ* Genebank in
170 Gatersleben, selected for maximized genetic diversity, were genotyped by using whole-genome
171 sequencing (WGS) data from Illumina short-read sequencing with 3x genome coverage (Milner et
172 al., 2019), and aligned to the barley MorexV2 reference genome (König et al., 2020; Mascher,
173 2020) (Supplemental Figure S1). A quality filter on 223 387 147 variants was applied with the
174 Plink 2.0 software as follows: missing values ≤ 0.02 and minor allele frequency (MAF) ≥ 0.05 .
175 After filtering, 949 174 high-quality variants remained and were used in GWAS analysis.

176 **4.5 Best linear unbiased estimator (BLUE)**

177 To obtain robust and unbiased phenotype means for the individual genotypes from the three
178 independent experiment repetitions, we used the Best linear unbiased estimator (BLUE)
179 (Henderson, 1975; Liu et al., 2008). BLUE were calculated by using the lme4 library for R using
180 the spore inoculation density as fixed factor.

181 **4.6 Genome-Wide Association Study**

182 GWAS for the seven traits was conducted with a Factored Spectrally Transformed Linear Mixed
183 Model using a kinship (K) matrix provided by the FaST-LMM program (*fastlmm* 0.5.5) (Lippert
184 et al., 2011; Listgarten et al., 2012). Suggestive threshold ($-\log_{10} P \geq 6.0$) was calculated based
185 on the formula $-\log_{10} (1/\text{number of independent SNPs})$ (Yang et al., 2014) and significance
186 threshold ($-\log_{10} P \geq 8.0$) for the identification of QTLs was calculated by using the Bonferroni
187 correction method (Hommel, 1988).

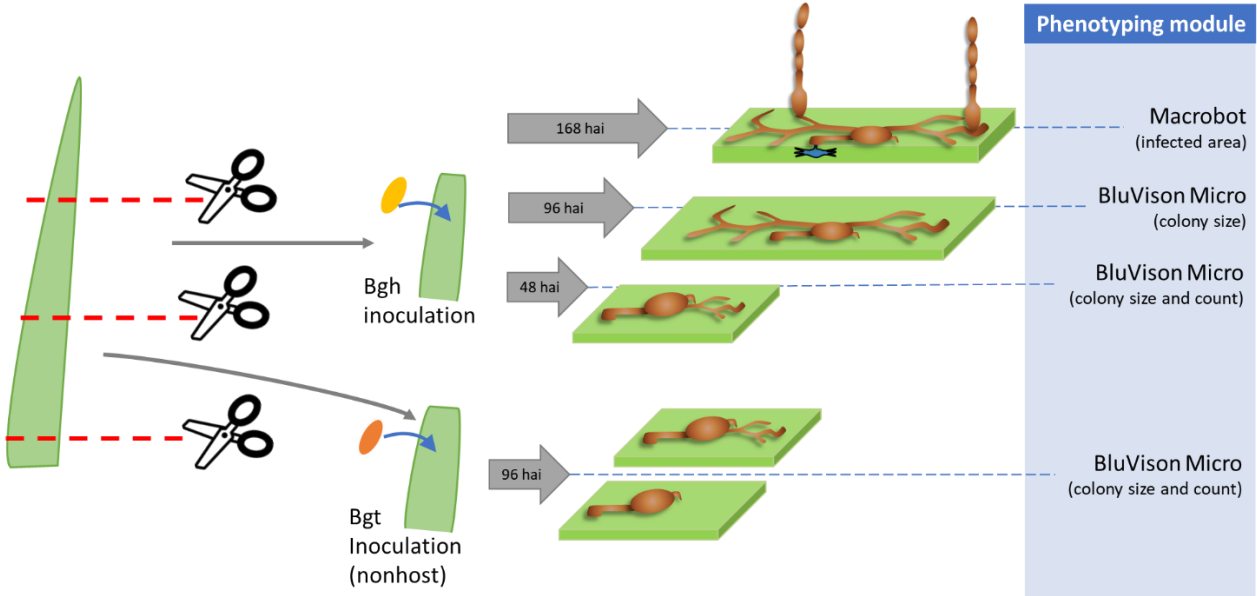
188 **4.7 Phenotype Preprocessing**

189 Six direct phenotypes and one derivative were derived for each leaf sample (Figure 1). The
190 microscopic phenotypes include normalized colony counts at 48 and 96 hours after infection (hai)
191 with the adapted pathogen (Bgh), and 96 hai with the non-adapted fungus (Bgt). In addition, one
192 macroscopic phenotype (infection spread at 168 hai) was included for comparison (Table 1).

193

194

195



196

197 **Figure 1.** Microscopic and macroscopic phenotypes derived from a single leaf. Up to eight barley
 198 plants of the same phenotype were grown for 14 days. Two segments from the second leaf of each
 199 plant were cut and inoculated with adapted (Bgh) or non-adapted (Bgt) pathogen. Samples for
 200 microscopy were collected at 48 and 96 hai.

201

202 **Table 1.** Analyzed phenotypes.

Phenotype	Phenotyping module	Scale	Pathogen	Time (hai)	Interaction type
Bgh_48hai_counts	BluVision Micro	Micro	Bgh	48	host
Bgh_48hai_size	BluVision Micro	Micro	Bgh	48	host
Bgh_96hai_size	BluVision Micro	Micro	Bgh	96	host
Bgt_96hai_counts	BluVision Micro	Micro	Bgt	96	nonhost
Bgt_96hai_counts_bin	BluVision Micro	Micro	Bgt	96	nonhost
Bgh_48-96hai_slope	BluVision Micro	Micro	Bgh	48-96	host
Bgh_168hai_area	Macrobot	Macro	Bgh	168	host

203

204

205 For colony mean size per leaf 48 and 96 hours after Bgh inoculation, the colony area was extracted
 206 from the segmented images with the OpenCV `contourArea()` function, and the BLUE was

207 calculated from the mean of three experiment repetitions for each barley genotype. The colony
208 sizes at both time points were used to calculate the slope of the growth curve, which was also used
209 as a phenotype in GWAS.

210 In addition to the quantitative phenotype (normalized colony counts) for the non-adapted pathogen
211 (96 hai Bgt), we also calculated a binary qualitative phenotype using a threshold for the normalized
212 colony count of 0.1. This approach reflects the qualitative nature of the NHR and allows for the
213 identification of major R-genes involved in this complex phenomenon.

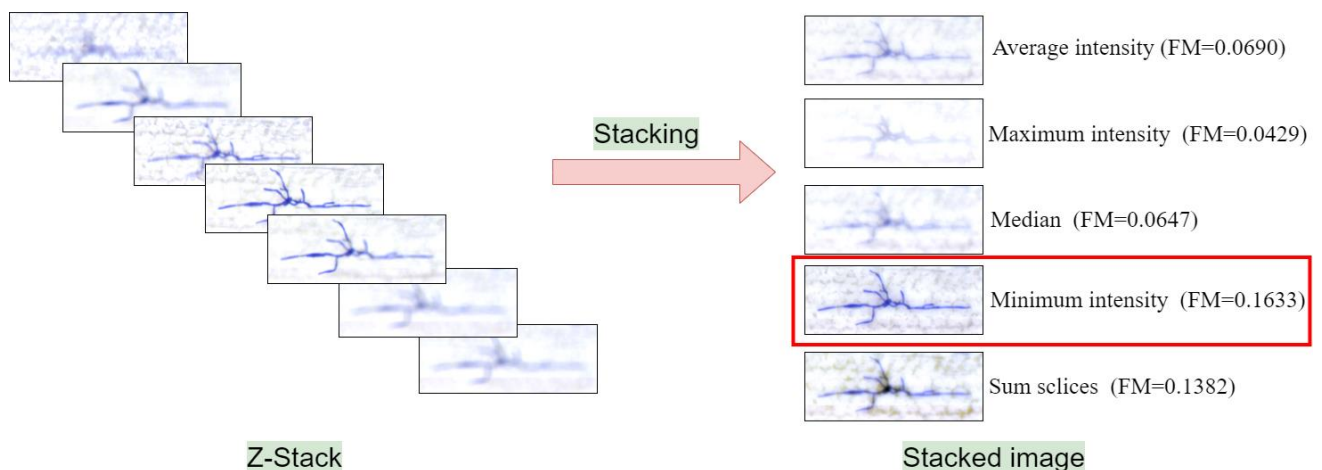
214 The macroscopic infection severity was calculated as the percentage of leaf area covered by the
215 powdery mildew colonies 168 hai using the *BluVision Macro* software (Lueck et al., 2020). A
216 mean of up to 8 technical replicates per accession in an experiment was used to calculate the BLUE
217 values.

218 5 Results

219 5.1 Image processing

220 5.1.1 Focus stacking

221 For finding the optimal focus stacking strategy of the multilevel CZI-images, we have tested five
222 different Z-projection methods included in the *Fiji* distribution package of *ImageJ v1.53* - Average
223 intensity (Khamfongkhrua et al., 2017), Maximum intensity (Sato et al., 1998), Minimum
224 intensity (Hayabuchi et al., 2011), Sum slices, Standard deviation and Median (Figure 2).



226 **Figure 2.** Comparing stacking algorithms. Five stacking algorithms were compared: Average
227 intensity, Maximum intensity, Median, Minimum intensity, Sum slices. The Minimum intensity
228 method achieved the highest quality measure (FM).

229 Furthermore, for each stacked image, the image Quality Measure (FM) has been computed and
230 compared (Table 2) (De and Masilamani, 2013). The minimum intensity projection method
231 achieved the best FM score in all tested cases and was selected for the image processing pipeline.

232

233 **Table 2.** *Intensity Z-projection methods compared on two image stacks*

Stack Nr.	Method	FM
Stack 1	average	0.0449
Stack 1	maximum intensity	0.0444
Stack 1	median	0.0456
Stack 1	minimum intensity	0.0825
Stack 1	sum slices	0.0691
Stack 2	average	0.0690
Stack 2	maximum intensity	0.0429
Stack 2	median	0.0647
Stack 2	minimum intensity	0.1633
Stack 2	sum slices	0.1382

234

235

236 5.1.2 Colony segmentation

237 The fungal colony images were extracted and classified in several steps. A significant challenge
238 was to design a reliable pipeline that tolerates staining quality and background variability without
239 losing too many positive objects.

240 First, the Z-stacked images were segmented to find the putative ROIs. Then, regions of interest
241 were extracted as a bounding box, and the image was classified into a positive or negative class.

242 Different common color spaces were tested: HSV, L*a*b, YCbCr, XYZ, AC1C2, YUV, I1I2I3
243 and YQ1Q2, in combination with different thresholding algorithms: Yen's maximum correlation
244 (Yen et al., 1995), Li's minimum cross-entropy method (Li and Lee, 1993; Li and Tam, 1998;
245 Sezgin and Sankur, 2004), Otsu (Otsu, 1979), Isodata (Ridler and Calvard, 1978), Mean (Glasbey,
246 1993), Minimum (Prewitt and Mendelsohn, 1966; Glasbey, 1993), Triangle (Zack et al., 1977),
247 Canny edge detector (Canny, 1986) (Table 3). Combining the Q2 channel from the YQ1Q2 color
248 space with Yen's thresholding generated the most reliable results. Using only a single-color
249 channel, we achieved a robust and reliable segmentation method that is insensitive to staining
250 variations and performs well on different sizes of the hyphae (36 to 72 hai).

251

252 **Table 3.** Segmentation methods for colony detection (image of 30 000 x 12 000 pixels containing
253 120 colonies). Comparison of the used software libraries, run-time per image and colony
254 segmentation performance.

Method	Library	Time(s)	Segmented colonies	Partial segmented colonies
Canny edge detector	OpenCV	6.5	30	109
Global thresholding	OpenCV	0.3	44	5
Adaptive Thresholding Mean	OpenCV	2.0	87	20
Adaptive Thresholding Gaussian	OpenCV	3.9	86	5
Otsu's Binarization	OpenCV	1.4	79	16
Li Minimum	scikit-image	112.0	4	22
Yen thresholding	scikit-image	81.0	16	19

255

256 A morphological closing operation was applied to the segmented binary images to close the gaps
257 that may lead to partial object extraction. Finally, a Moore-Neighbour tracing algorithm
258 (Weisstein, 2021) was used to extract the contours of the binary image for colony classification.

259

260 5.2 Machine learning

261 5.2.1 Training data set

262 Bgh inoculated barley leaves were Coomassie-stained at 36-72 hai and scanned with the
263 *AxioScan.Z1* system. The multilevel images were processed as described above. The putative ROIs
264 were extracted with a bounding box and saved as separate images. The images were manually
265 curated, and about 10 000 ROI containing fungal colonies were selected. Another 8 000 images
266 without any fungal structures but other objects and artifacts were selected as negative training data.
267 Finally, a small training set with 3 200 images per class was extracted from the large training set
268 to study the prediction performance based on the training set size.

269 Both datasets were split randomly into 75% of the images for training the models and 25% for
270 validation and evaluation. Since the Convolutional Neuronal Network (CNN) approach requires
271 identical dimensions of the training images, they were resized to 150 x 350 pixel, the mean ROI
272 size of the particular data set.

273 5.2.2 Classification using handcrafted features

274 Manual selection of features for building a reliable classifier is still a widely used approach that,
275 in some cases, may outperform more sophisticated methods (Lück et al., 2020). However, the
276 success of this approach strongly depends on the selection of informative and robust features. In
277 our case, of particular importance was to select color- and scale-invariant features because of the
278 high staining intensity- and colony size variation.

279 The contours received after the segmentation step were first filtered using geometrical features
280 (Table 4) to reduce artifacts and non-fungal structures.

281

282 **Table 4.** Object size parameters for filtering colonies from the artifacts. Minimum and maximum
283 thresholds for colonies are indicated.

Feature	Minimum pixel values	Minimum pixel values
Width	100	1400
Height	100	800
Aspect ratio	0.5	10.0
Area	1000	30000

284

285 Then, five scale- and color-invariant features (Histogram of oriented Gaussians (Dalal and Triggs,
286 2005), Local binary pattern (Dong-chen and Li, 1990; Wang and He, 1990), Haralick (Haralick et
287 al., 1973), Zernike Moments (Tahmasbi et al., 2011), Parameter-free threshold adjacency statistics
288 (Coelho et al., 2010); Table 5) were extracted with the *mahotas* and *scikit-image* library, and a
289 random forest classifier with 80 trees was trained with the two training sets (3 200 and 10 000
290 images per class).

291

292 **Table 5.** Edge and texture descriptors.

Name	Abbreviation	Descriptor
Histogram of oriented Gaussians	HOG	Edge
Local binary pattern	LB	Texture
Haralick	HA	Texture
Zernike Moments	ZM	Shape
Parameter-free threshold adjacency statistics	PFTAS	Texture

293

294 Finally, the performance of *Accuracy*, *Precision*, and *Recall* scores were calculated according to
295 Equation 1 and shown in Tables 6 and 7.

296

297

$$Accuracy = \frac{TP + TN}{TP + FP + FN + TN}$$

298

$$Precision = \frac{TP}{TP + FP}$$

299

$$Recall = \frac{TP}{TP + FN}$$

300 **Equation 1.** *Accuracy, Precision, and Recall scores calculation. TP – true positive, TN – true*
301 *negative, FP – false positive, FN – false negative (according to the ground thought, see Validation*
302 *chapter).*

303

304 **Table 6.** *Random Forest model for image features. Ca. 3 200 objects per class. Average of 10*
305 *independent trainings.*

Method	Precision	SD	Recall	SD	Accuracy	SD
HOG	0.8493	0.0097	0.8895	0.0110	0.8634	0.0053
LB	0.9346	0.0076	0.9547	0.0077	0.9429	0.0048
HA	0.9075	0.0100	0.9216	0.0071	0.9109	0.0056
ZM	0.7816	0.0144	0.8239	0.0075	0.7919	0.0066
PFTAS	0.8821	0.0070	0.9288	0.0082	0.9000	0.0042

306

307 **Table 7.** *Random Forest model for image features. Ca. 10 000 objects per class. Average of 10*
308 *independent trainings.*

Method	Precision	SD	Recall	SD	Accuracy	SD
HOG	0.8472	0.0081	0.8893	0.0080	0.8641	0.0059
LB	0.9346	0.0076	0.9547	0.0077	0.9429	0.0048
HA	0.9088	0.0057	0.9311	0.0059	0.9186	0.0046
ZM	0.6841	0.0116	0.7419	0.0120	0.7018	0.0064
PFTAS	0.8516	0.0082	0.8830	0.0055	0.8653	0.0056

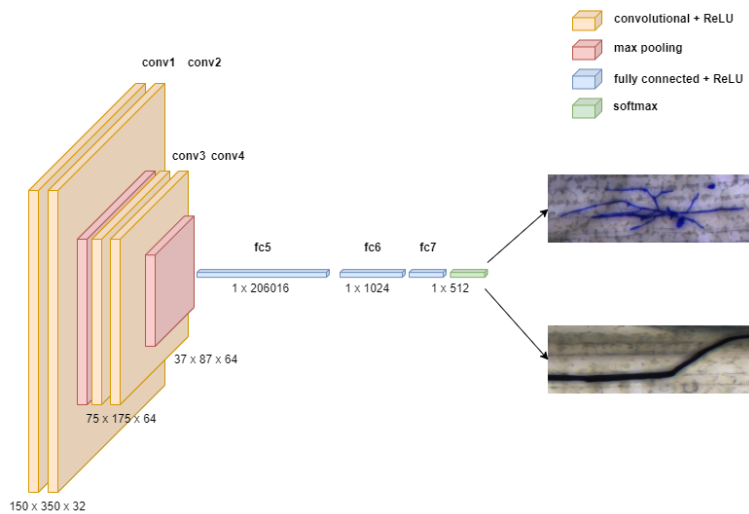
309

310

311

312 5.2.3 Convolutional neural network

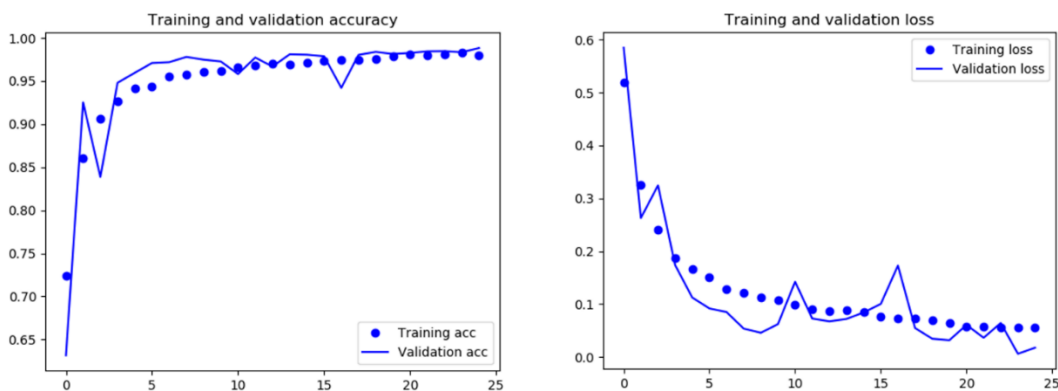
313 We implemented a standard convolutional neural network (Figure 3) with dropout 0.2 and trained
314 two training sets with different sizes (ca. 3 200 and 10 000 images per class) over 25 epochs. We
315 used rectified linear activation function during training, followed by a final SoftMax activation
316 function to receive the probability distribution over the classes. In addition, we used the stochastic
317 gradient descent optimizer with a learning rate of 0.01, batch size of 32, and momentum of 0.9 to
318 allow one training image to pass through the neural network at a time and update the weights for
319 each layer. The final validation accuracy of the model was 97.13% (Figure 4).



320

321 **Figure 3.** The structure of a convolutional neural network consists of convolutional, pooling, and
322 fully connected layers.

323



324

325 **Figure 4.** Training and validation accuracy of the model CNN model trained with ca. 10 000
326 positive images.

327

328 **5.3 Validation**

329 One hundred twenty colonies were labeled manually as ground truth by a domain expert. When
330 comparing the handcrafted features random forest models trained on 3 200 images per class, the
331 local binary pattern feature reached the highest accuracy and precision (>0.94 ; Table 6) but failed
332 when using the model on the validation set (False negative $> 90\%$; Table 8). This is usually an
333 indication of model overfitting resulting in a too stringent prediction or a poor capability to deal
334 with new data. This example demonstrates how misleading the theoretical performance metrics
335 can be if used solely without validating the model with new experimental data. Re-testing all
336 previously built models with a new validation data set revealed the *Parameter-free threshold*
337 *adjacency statistics* (PFTAS) and *haralick* (HA) as best performing (True positives $> 88\%$, False
338 positives $< 10\%$). Furthermore, a new model based on the combination of both methods
339 significantly improved the accuracy ending up with 91% true positives, 9 % false negatives, and
340 only 1% false positives objects on the validation set (Table 8).

341 However, increasing the training data size to 10 000 images did not significantly improve the
342 handcrafted feature-based model results, which indicates that the learning curve reached the
343 plateau (Table 7). In contrast, the CNN models gain from big data and larger training sets. By
344 using the dataset with 10 000 images, the true positive rate increases by 3.3% to 89.1%, and the
345 false-positive rate decreases to 0.0% (with the prediction accuracy score set to the maximum of
346 1.0) (Table 8). Loosening the prediction accuracy score to 0.9 helped achieve a high-performance
347 CNN model with over 98% true positive rate and below 3% false-positive rate. In direct
348 comparison, the CNN model shows 10% better accuracy in predicting hyphal objects than the top
349 handcrafted RF-model while keeping the false positive 7% lower (Table 8).

350 Comparing our best CNN model with a 0.9 prediction score against the HyphArea software, our
351 proposed software improved the true positive prediction by more than 70% and decreased the false
352 positive rate by 10 % (Table 8).

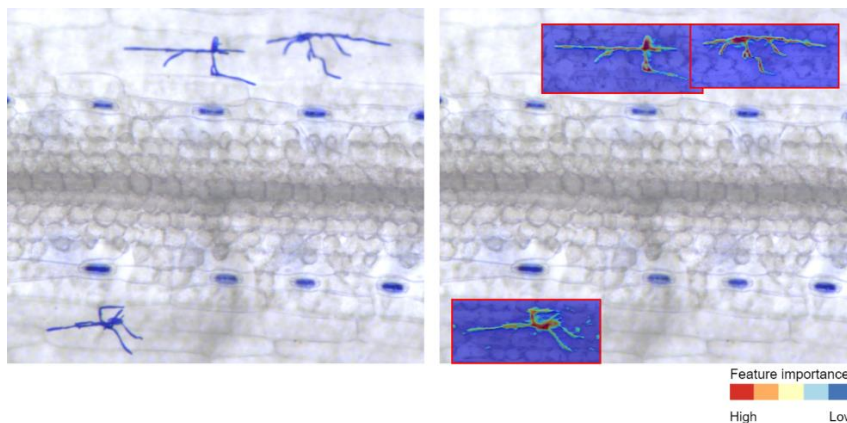
353 **5.3.1 Run-time and parallel processing**

354 Considering the aim to do high-throughput microscopy image analysis, we invested in optimizing
355 the algorithm for run-time per image. Besides other improvements, using numerical Python
356 libraries, which allows efficient numerical calculations on multi-dimensional arrays, and
357 parallelizing the processes with the *joblib* library (Python) led to a significant speed gain. As a

358 result, *BluVision Micro* performed up to 30 times faster than the previous HyphArea software in
359 analyzing pyramid images of average size 30 000 x 25 000 pixels. On an Intel® Core™ i7-9700
360 CPU 3.00 GHz with 64-Bit Windows 10 operating system and NVIDIA TITAN X GPU support,
361 the software run time takes about 60 seconds per slide containing two images of size 30 000 x 25
362 000 pixels, which is 3-5 faster than the image acquisition time, this allowing real-time analysis.

363 5.3.2 Feature Visualization

364 Visualizing the CNN predictions becomes crucial because of the increasing requirements for
365 transparency of the artificial intelligence prediction models. However, the availability of
366 visualization options was limited until recently, when several such tools were developed. To
367 examine the *BluVision Micro* CNN model's prediction and facilitate debugging, we used *Keras*
368 *Visualization Toolkit* (Zhou et al., 2015) to generate heatmap images to visualize the *Class*
369 *activation maps* for the fungal structures. The resulting heatmaps correctly represented the area
370 covered by the fungal microcolonies (Figure 5).



371

372 **Figure 5.** Heatmap visualization of the class activation map for fungal structures. The left image
373 represents the raw image data, and on the right are the regions of interest detected by the software
374 (red border rectangle) with hyphae segmentation. The example clearly shows that the CNN model
375 localizes the fungal colony with high probability (red colors), as the probability in the background
376 drops significantly (blue colors).

377

378 5.4 Application

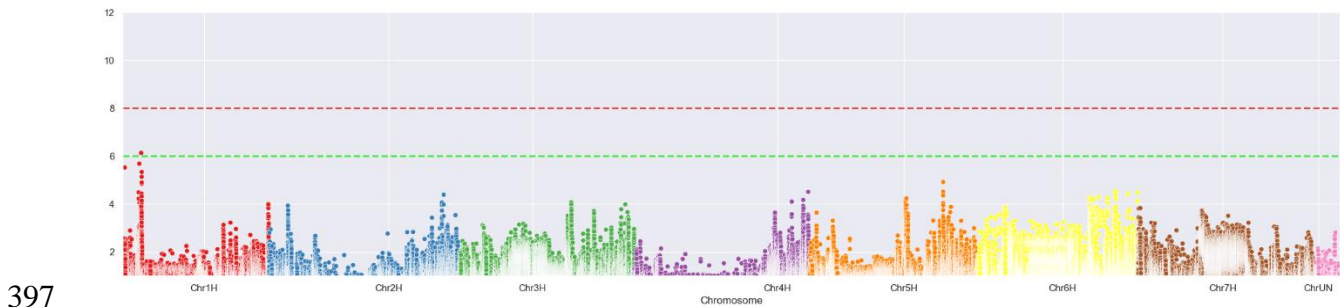
379 5.4.1 Genome-wide association scans (GWAS)

380 The experiment design (Figure 1) allowed the quantification of multiple phenotypes (Table 1)
381 from a single leaf. They cover the response to adapted and non-adapted pathogens on microscopic

382 and macroscopic levels. The precise phenotypic data was combined with the dense SNP data (949
383 174 quality SNPs) for GWAS for resistance-associated markers.

384 Since the study aims to provide proof of concept and application examples, the number of tested
385 genotypes was 200, which is on the lower end to detect significant marker-trait associations (MTA)
386 in genetically diverse materials. Nevertheless, we were able to identify eight loci containing MTAs
387 with statistical significance above the suggestive threshold ($-\log_{10} P \geq 6.0$) and three loci with
388 MTA above the significance threshold ($-\log_{10} P \geq 8.0$). Surprisingly, the novel nonhost resistance
389 phenotypes achieved the highest association peaks leading, besides finding other MTAs, to the re-
390 discovering one of the very few published nonhost resistance QTL (Romero et al., 2018) (Figure
391 6E). All discovered significant MTAs and the genes located in the underlying genomic region are
392 listed in Supplemental Tables MTA_list_[phenotype] and Gene_list_[phenotype].

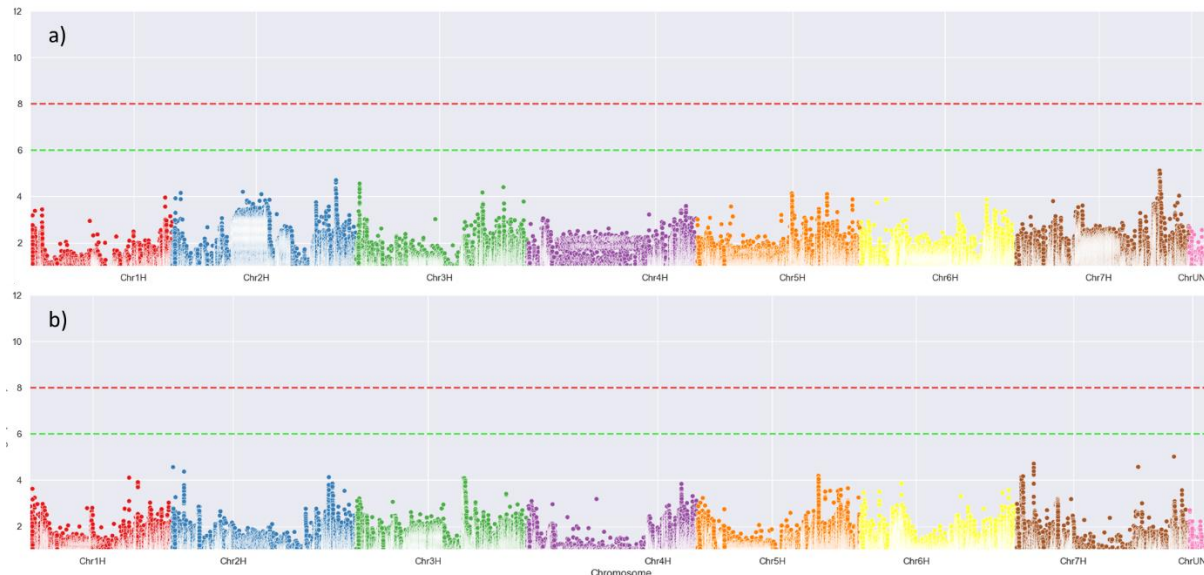
393 The macroscopic phenotyping (Bgh_168hai_area) (Figure 6) suffered from some barley
394 genotypes' apparent tendency to accelerate senescence in detached leaf assay and formation of
395 physiological necrotic flecks that prevent the spreading of the disease and compromise the
396 phenotyping.



398 **Figure 6.** Manhattan plot of the $[-\log_{10}]$ transformed p -values of the genomic regions associated
399 with the macroscopic phenotype of infected leaf area at 168 hai Bgh. Green dashed line –
400 suggestive threshold, red dashed line – significance threshold.

401
402 The colony size-based phenotypes (Bgh_48hai_size, Bgh_96hai_size) (Figure 7a and 7b) did not
403 deliver significant MTAs (Figure 7). This is not unexpected because a natural resistance based on
404 fungal growth retardation, to our best knowledge, is not yet described in the literature, not at last
405 because of the lack of screening methods. However, such phenotypes likely exist, and a systematic
406 screen of diverse plant genotypes may help discover them.

407

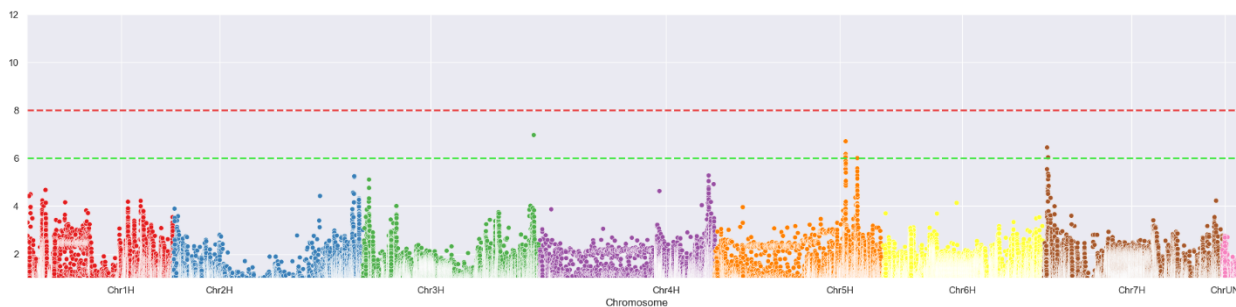


408

409 **Figure 7.** Manhattan plot of the $[-\log_{10}]$ transformed p -values of the genomic regions associated
410 with colony size-based phenotypes a) Bgh colony size at 48hai, b) Bgh colony size at 96hai. Green
411 dashed line – suggestive threshold, red dashed line – significance threshold.

412

413 Also, as expected, the colony counts delivered some significant MTAs (Figure 8), since the
414 penetration resistance against powdery mildew fungus, which efficiently reduces the number of
415 successful infection events, is widespread in barley. However, the MTA reached only the
416 suggestive threshold, not the significance threshold, which is pretty high because of the large
417 number of SNP included in the analysis (~1 000 000).

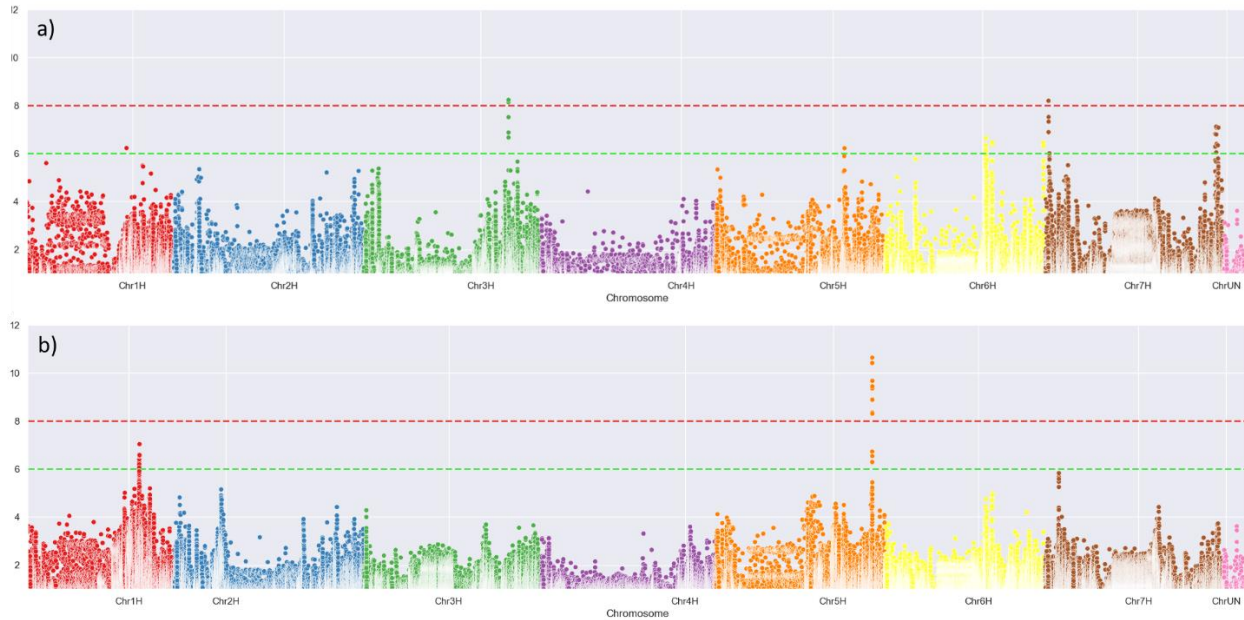


418

419 **Figure 8** Manhattan plot of the $[-\log_{10}]$ transformed p -values of the genomic regions associated
420 with normalized Bgh colony counts at 48 hai. Green dashed line – suggestive threshold, red dashed
421 line – significance threshold.

422

423 The high sensitivity and performance of the system allowed approaching an exciting novel
424 phenotype – quantifying the rare cryptic infection of non-adapted pathogens, which allowed the
425 discovery of genes and loci associated with this most valuable type of resistance (Figure 9).



426

427 **Figure 9.** Manhattan plot of the $[-\log_{10}]$ transformed p -values of the genomic regions associated
428 with normalized Bgt colony counts (a), and binarized susceptibility phenotype (b) at 96 hai. Green
429 dashed line – suggestive threshold, red dashed line – significance threshold.

430

431 Surprisingly, this novel phenotype delivered the most significant MTAs, indicating the
432 involvement of major-effect genes. Furthermore, the MTA with the absolute most significant p -
433 value in the entire experiment pointed precisely to the peak marker position found by (Romero et
434 al., 2018) and probably conferred by one or both of the Receptor-like kinases located in this region.

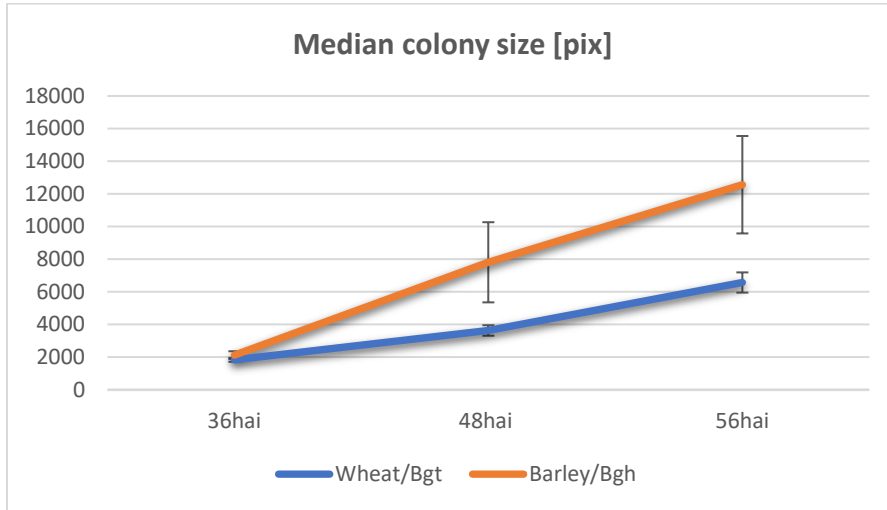
435

436 5.4.2 Pathogen growth curves

437 The *BluVision Micro* platform provides the possibility to measure precisely, and in high-
438 throughput, the area of the secondary hyphae of the powdery mildew colonies. This opens new
439 phenotyping options, hardly possible with the previously existing manual tools. For instance,
440 measuring the colony size at a specific time point after inoculation may reveal plant defense
441 mechanisms that rely on retarding the pathogen growth, e.g., cutting the nutrient support for the

442 fungus or late activation of cell death mechanisms. Furthermore, acquiring colony size data on
443 multiple time points will allow for building growth curves for the pathogen (Figure 10).

444

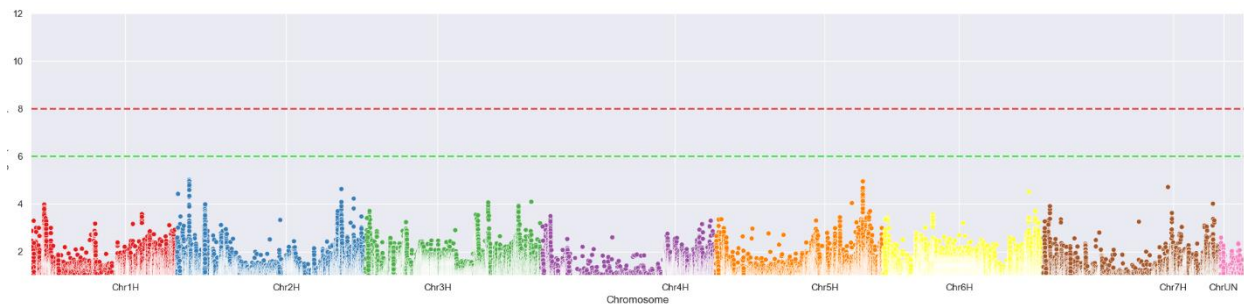


445

446 **Figure 10.** Growth curve of two adapted powdery mildew species on wheat and barley,
447 respectively.

448

449 We used the median Bgh colony sizes at 48 and 96 hai on the 200 barley genotypes to build
450 genotype-specific growth slopes and used them as a phenotype in GWAS. As for the direct colony
451 size phenotypes, none of the MTAs reached even the suggestive threshold with the derivative one.
452 Nevertheless, this novel phenotyping method may reveal plant resistance that works by retarding
453 the pathogen growth. Also, it can be a valuable tool in comparing the fitness of different pathogen
454 races.



455

456 **Figure 11.** Manhattan plot of the $[-\log_{10}]$ transformed p-values of the genomic regions associated
457 with the slope of the growth curve of Bgh at 48-96 hai. Green dashed line – suggestive threshold,
458 red dashed line – significance threshold.

459

460 **6 Discussion**

461 The need for automated microscopic phenotyping of plant-pathogen interactions became apparent
462 with increasing the available genetic and genomics resources and the pursuit of finding and
463 validating the functions of the myriad of genes putatively involved in the complex disease
464 resistance phenotype. HyphArea was the first software implementation to detect and quantify
465 secondary hyphae of *B. graminis* on barley and wheat. The tool pioneered establishing a high-
466 throughput platform for plant-pathogen interaction phenotyping on a microscopic level allowed
467 access to novel phenotypes such as quantification for the fungal hyphae area. However, the high
468 sensitivity and specificity levels of the HyphArea Tool demonstrated in (Seiffert and Schweizer,
469 2005; Baum et al., 2011) was often difficult to reach due to differences in the material quality and
470 variations of the sample preparations.

471 Besides the image analysis, the extended use of the HyphArea revealed issues with the handling
472 and processing of the raw data. The acquired image data were exported as individual camera
473 frames (tiles) and stored in separate TIFF files. This step simplifies the image data processing and
474 avoids using proprietary file formats but results in a massive expansion of the file number ($>10^6$
475 files for a large screen), thus approaching the limits of the used hardware and software. Finally,
476 the high run time of the HyphArea renders it less appropriate for high-throughput phenotyping
477 screenings.

478 Benefiting from the accumulated experience and using newer high-throughput automated
479 microscopy and software techniques, we have developed a completely new system for microscopy-
480 based phenotyping. We decided to opt for a modular, machine learning-based software that works
481 directly with different image data types, including complex pyramid files and multimodal images,
482 and it is easily adaptable and extendable with modules for additional phenotypes.

483 Handcrafted features, if chosen correctly, can provide acceptable performance in cases where only
484 small ($< 5\ 000$ images per class) training sets are available. However, using more training data for
485 the handcrafted features approach does not further increase the performance, showing that we have
486 reached the methods' limits in this case. For higher accuracy and larger training sets ($> 5\ 000$
487 images per class), we recommend using a CNN, which is a major advantage is extracting the
488 probability for each class and use it as a parameter for predictions.

489 The BluVision system can derive precise microscopy phenotypes for different large-scale studies,
490 such as screening of Genbank material, crossing populations, mutant collections, breeding
491 material, and others, at both host and pathogen sides. In this study, we have used the system to
492 screen 200 highly genetically diverse barley genotypes for interaction phenotypes with adapted
493 and non-adapted powdery mildew fungi. The system was confirmed to deliver accurate, sensitive,
494 and reproducible results. We have used them to scan for marker-trait associations in the barley
495 genome, discover several novel loci, and confirm already known. Noticeably, we were able to re-
496 discover one of the first published nonhost-resistance QTL, described by (Romero et al., 2018),
497 which confirms the system's applicability for studies aiming to discover genes involved in this
498 precious but hardly accessible trait – the nonhost resistance. Furthermore, the systems allow high-
499 throughput studies of previously extremely laborious phenotypes, such as precise colony area and
500 scoring pre- and post-haustorial defense reactions. By using other (not yet published) dedicated
501 modules, the BluVision platform can also detect the presence of fungal haustoria in reporter gene
502 (GUS) expressing cells, thus enabling high-throughput transfection assays for disease resistance-
503 related genes. The open-source software system allows the development of specific modules for
504 other microscopic phenotypes. The framework is hardware-independent and adaptable to different
505 commercial imaging systems based on the Digital Imaging and Communications in Medicine
506 (DICOM) standard, such as Zeiss Axionscan and Leica Aperio systems.

507 Thus, we have developed an open-source, extendable, high-throughput automated microscopy
508 system for analyzing microscopic phenotypes. Furthermore, we have validated the system's
509 performance in disease resistance screens of genetically diverse barley material and demonstrated
510 that the phenotypic data could be used for Genome-wide associations scans (GWAS), discovering
511 several resistance-associated loci, including conferring nonhost resistance.

512

513 **7 Acknowledgments**

514 This work was initiated and actively supported by Patrick Schweizer, who passed away in March
515 2018. The authors dedicate this work to his memory. Further on, we would like to acknowledge
516 the following colleagues from IPK Gatersleben: Nils Stein, Martin Marcher, Murukarthick
517 Jayakodi for the genotypic data for the 200 barley accessions; Andreas Börner for providing single-
518 seed-descent seed material for the experiments; and André Fessel and Gabriele Brantin for the

519 technical help. The work was supported by IPK Gatersleben and the German Ministry of Education
520 and Research (BMBF) with grants FKZ 031A053 (DPPN) and FKZ 031B0184 (GeneBank 2.0).

521 **8 Author Contribution**

522 SL and DD wrote the manuscript, SL performed the image analysis, computer model development,
523 and GWAS, DD designed the research and performed the biological experiments.

524

525 **9 Data Availability**

526 *BluVision Micro* ships with Attribution-NonCommercial 4.0 International license (CC BY-NC
527 4.0). The open-source code is accessible at <https://github.com/snowformatics/BluVisionMicro>.
528 Image training sets are available at the electronic Data Archive Library (e!DAL) (link with the
529 next manuscript revision).

530

531

532 10 References

- 533 **Baum T, Navarro-Quezada A, Knogge W, Douchkov D, Schweizer P, Seiffert U** (2011)
534 HyphArea-Automated analysis of spatiotemporal fungal patterns. *Journal of Plant*
535 *Physiology* **168**: 72-78
- 536 **Bettgenhaeuser J, Hernandez-Pinzon I, Dawson AM, Gardiner M, Green P, Taylor J,**
537 **Smoker M, Ferguson JN, Emmrich P, Hubbard A, Bayles R, Waugh R, Steffenson**
538 **BJ, Wulff BBH, Dreiseitl A, Ward ER, Moscou MJ** (2021) The barley immune receptor
539 Mla recognizes multiple pathogens and contributes to host range dynamics. *Nature*
540 *Communications* **12**
- 541 **Bourras S, Kunz L, Xue MF, Praz CR, Muller MC, Kalin C, Schläfli M, Ackermann P,**
542 **Fluckiger S, Parlange F, Menardo F, Schaefer LK, Ben-David R, Roffler S,**
543 **Oberhaensli S, Widrig V, Lindner S, Isaksson J, Wicker T, Yu DZ, Keller B** (2019)
544 The AvrPm3-Pm3 effector-NLR interactions control both race-specific resistance and
545 host-specificity of cereal mildews on wheat. *Nature Communications* **10**
- 546 **Canny J** (1986) A computational approach to edge detection. *IEEE Trans Pattern Anal Mach Intell*
547 **8**: 679-698
- 548 **Coelho LP, Ahmed A, Arnold A, Kangas J, Sheikh A-S, Xing EP, Cohen WW, Murphy RF**
549 (2010) Structured Literature Image Finder: Extracting Information from Text and Images
550 in Biomedical Literature. *In*. Springer Berlin Heidelberg, Berlin, Heidelberg, pp 23-32
- 551 **Dalal N, Triggs B** (2005) Histograms of Oriented Gradients for Human Detection. *In* Proceedings
552 of the 2005 IEEE Computer Society Conference on Computer Vision and Pattern
553 Recognition (CVPR'05) - Volume 1 - Volume 01. IEEE Computer Society, pp 886-893
- 554 **De K, Masilamani V** (2013) Image Sharpness Measure for Blurred Images in Frequency Domain.
555 *Procedia Engineering* **64**: 149-158
- 556 **Dong-chen H, Li W** (1990) Texture Unit, Texture Spectrum, And Texture Analysis. *IEEE*
557 *Transactions on Geoscience and Remote Sensing* **28**: 509-512
- 558 **Douchkov D, Luck S, Johrde A, Nowara D, Himmelbach A, Rajaraman J, Stein N, Sharma**
559 **R, Kilian B, Schweizer P** (2014) Discovery of genes affecting resistance of barley to
560 adapted and non-adapted powdery mildew fungi. *Genome Biology* **15**
- 561 **FAO** (2020) FAO launches 2020 as the UN's International Year of Plant Health. *In*, Vol 2020.
562 FAI, <http://www.fao.org/news/story/en/item/1253551/icode/>
- 563 **Glasbey CA** (1993) An Analysis of Histogram-Based Thresholding Algorithms. *CVGIP:*
564 *Graphical Models and Image Processing* **55**: 532-537
- 565 **Haralick RM, Shanmugam K, Dinstein I** (1973) Textural Features for Image Classification. *Ieee*
566 *Transactions on Systems Man and Cybernetics* **Smc3**: 610-621
- 567 **Hayabuchi Y, Inoue M, Watanabe N, Sakata M, Nabo MMH, Kagami S** (2011) Minimum-
568 intensity projection of multidetector-row computed tomography for assessment of
569 pulmonary hypertension in children with congenital heart disease. *International Journal of*
570 *Cardiology* **149**: 192-198

- 571 **Henderson CR** (1975) Best Linear Unbiased Estimation and Prediction under a Selection Model.
572 *Biometrics* **31**: 423-447
- 573 **Hinton G** (1999) Unsupervised Learning: Foundations of Neural Computation. *In*. The MIT Press
- 574 **Hommel G** (1988) A Stagewise Rejective Multiple Test Procedure Based on a Modified
575 Bonferroni Test. *Biometrika* **75**: 383-386
- 576 **Khamfongkhrua C, Thongsawad S, Tannanonta C, Chamchod S** (2017) Comparison of CT
577 images with average intensity projection, free breathing, and mid-ventilation for dose
578 calculation in lung cancer. *Journal of applied clinical medical physics* **18**: 26-36
- 579 **König P, Beier S, Basterrechea M, Schüler D, Arend D, Mascher M, Stein N, Scholz U, Lange
580 M** (2020) BRIDGE – A Visual Analytics Web Tool for Barley Genebank Genomics.
581 *Frontiers in Plant Science* **11**
- 582 **Li CH, Lee CK** (1993) Minimum cross entropy thresholding. *Pattern Recognition* **26**: 617-625
- 583 **Li CH, Tam PKS** (1998) An iterative algorithm for minimum cross entropy thresholding. *Pattern
584 Recognition Letters* **19**: 771-776
- 585 **Lin W, Hasenstab K, Moura Cunha G, Schwartzman A** (2020) Comparison of handcrafted
586 features and convolutional neural networks for liver MR image adequacy assessment.
587 *Scientific Reports* **10**: 20336
- 588 **Lippert C, Listgarten J, Liu Y, Kadie CM, Davidson RI, Heckerman D** (2011) FaST linear
589 mixed models for genome-wide association studies. *Nature Methods* **8**: 833-835
- 590 **Listgarten J, Lippert C, Kadie CM, Davidson RI, Eskin E, Heckerman D** (2012) Improved
591 linear mixed models for genome-wide association studies. *Nature Methods* **9**: 525-526
- 592 **Liu X-Q, Rong J-Y, Liu X-Y** (2008) Best linear unbiased prediction for linear combinations in
593 general mixed linear models. *Journal of Multivariate Analysis* **99**: 1503-1517
- 594 **Lück S, Strickert M, Lorbeer M, Melchert F, Backhaus A, Kiliass D, Seiffert U, Douchkov D
595** (2020) “Macrobot”: An Automated Segmentation-Based System for Powdery Mildew
596 Disease Quantification. *Plant Phenomics* **2020**: 5839856
- 597 **Lueck S, Beukert U, Douchkov D** (2020) BluVision Macro - a software for automated powdery
598 mildew and rust disease quantification on detached leaves. *The Journal of Open Source
599 Software* **5(51)**
- 600 **Mascher M** (2020) Assembly, annotation and analysis of the barley (*Hordeum vulgare* L.) pan-
601 genome. *In*. e!DAL - Plant Genomics and Phenomics Research Data Repository (PGP),
602 IPK Gatersleben, Seeland OT Gatersleben, Corrensstraße 3, 06466, Germany
- 603 **Milner SG, Jost M, Taketa S, Mazón ER, Himmelbach A, Oppermann M, Weise S, Knüpfper
604 H, Basterrechea M, König P, Schüler D, Sharma R, Pasam RK, Rutten T, Guo G, Xu
605 D, Zhang J, Herren G, Müller T, Krattinger SG, Keller B, Jiang Y, González MY,
606 Zhao Y, Habekuß A, Färber S, Ordon F, Lange M, Börner A, Graner A, Reif JC,
607 Scholz U, Mascher M, Stein N** (2019) Genebank genomics highlights the diversity of a
608 global barley collection. *Nature Genetics* **51**: 319-326
- 609 **Mitchell TM** (1997) *Machine Learning*,

- 610 **Otsu N** (1979) A Threshold Selection Method from Gray-Level Histograms. IEEE Transactions
611 on Systems, Man, and Cybernetics **9**: 62-66
- 612 **Panstruga R, Dodds PN** (2009) Terrific Protein Traffic: The Mystery of Effector Protein Delivery
613 by Filamentous Plant Pathogens. Science **324**: 748-750
- 614 **Prewitt JMS, Mendelsohn ML** (1966) THE ANALYSIS OF CELL IMAGES*. Annals of the
615 New York Academy of Sciences **128**: 1035-1053
- 616 **Ridler TW, Calvard S** (1978) Picture Thresholding Using an Iterative Selection Method. IEEE
617 Transactions on Systems, Man, and Cybernetics **8**: 630-632
- 618 **Romero CCT, Vermeulen JP, Vels A, Himmelbach A, Mascher M, Niks RE** (2018) Mapping
619 resistance to powdery mildew in barley reveals a large-effect nonhost resistance QTL.
620 Theoretical and Applied Genetics **131**: 1031-1045
- 621 **Russell SJ** (2010) Artificial intelligence : a modern approach. Third edition. Upper Saddle River,
622 N.J. : Prentice Hall, [2010] ©2010
- 623 **Sato Y, Shiraga N, Nakajima S, Tamura S, Kikinis R** (1998) Local Maximum Intensity
624 Projection (LMIP: A New Rendering Method for Vascular Visualization. Journal of
625 Computer Assisted Tomography **22**
- 626 **Seiffert U, Schweizer P** (2005) A pattern recognition tool for quantitative analysis of in planta
627 hyphal growth of powdery mildew fungi. Molecular Plant-Microbe Interactions **18**: 906-
628 912
- 629 **Sezgin M, Sankur B** (2004) Survey over image thresholding techniques and quantitative
630 performance evaluation. Journal of Electronic Imaging **13**: 146-168
- 631 **Spanu P, Kamper J** (2010) Genomics of biotrophy in fungi and oomycetes - emerging patterns.
632 Current Opinion in Plant Biology **13**: 409-414
- 633 **Stockman G, Shapiro LG** (2001) Computer Vision. Prentice Hall PTR
- 634 **Tahmasbi A, Saki F, Shokouhi SB** (2011) Classification of benign and malignant masses based
635 on Zernike moments. Comput. Biol. Med. **41**: 726–735
- 636 **Voulodimos A, Doulamis N, Doulamis A, Protopapadakis E** (2018) Deep Learning for
637 Computer Vision: A Brief Review. Computational Intelligence and Neuroscience **2018**:
638 7068349
- 639 **Wang L, He D-C** (1990) Texture classification using texture spectrum. Pattern Recognition **23**:
640 905-910
- 641 **Weisstein EW** (2021) Moore Neighborhood *In* MathWorld - A Wolfram Web Resource, Vol
642 2021, MathWorld - A Wolfram Web Resource.
643 <https://mathworld.wolfram.com/MooreNeighborhood.html>
- 644 **Yang W, Guo Z, Huang C, Duan L, Chen G, Jiang N, Fang W, Feng H, Xie W, Lian X, Wang
645 G, Luo Q, Zhang Q, Liu Q, Xiong L** (2014) Combining high-throughput phenotyping
646 and genome-wide association studies to reveal natural genetic variation in rice. Nature
647 Communications **5**: 5087
- 648 **Yen JC, Chang FJ, Chang S** (1995) A new criterion for automatic multilevel thresholding. IEEE
649 Trans Image Process **4**: 370-378

- 650 **Zack GW, Rogers WE, Latt SA** (1977) Automatic measurement of sister chromatid exchange
651 frequency. *J Histochem Cytochem* **25**: 741-753
- 652 **Zheng A, Casari A** (2018) *Feature Engineering for Machine Learning: Principles and Techniques*
653 *for Data Scientists*. O'Reilly Media, Inc.
- 654 **Zhou B, Khosla A, Lapedriza A, Oliva A, Torralba A** (2015) Learning Deep Features for
655 Discriminative Localization,
656
657